Accepted Manuscript

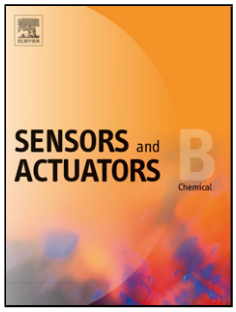

Title: Numerical prototyping of lateral flow biosensors

Author: Federico Schaumburg Pablo A. Kler Claudio L.A. Berli

PII: S0925-4005(17)32370-5
DOI: https://doi.org/doi:10.1016/j.snb.2017.12.044
Reference: SNB 23732

To appear in: *Sensors and Actuators B*

Received date: 20-9-2017
Revised date: 30-11-2017
Accepted date: 8-12-2017

Please cite this article as: Federico Schaumburg, Pablo A. Kler, Claudio L.A. Berli, Numerical prototyping of lateral flow biosensors, *<![CDATA[Sensors & Actuators: B. Chemical]]>* (2017), https://doi.org/10.1016/j.snb.2017.12.044

This is a PDF file of an unedited manuscript that has been accepted for publication. As a service to our customers we are providing this early version of the manuscript. The manuscript will undergo copyediting, typesetting, and review of the resulting proof before it is published in its final form. Please note that during the production process errors may be discovered which could affect the content, and all legal disclaimers that apply to the journal pertain.

ACCEPTED MANUSCRIPT

Numerical prototyping of lateral flow biosensors

Federico Schaumburg[a], Pablo A. Kler[b,c], Claudio L. A. Berli[a]

[a] *Instituto de Desarrollo Tecnológico para la Industria Química (INTEC, UNL–CONICET). Colectora RN 168 Km 472. S3000GLN Santa Fe, Argentina.*
[b] *Centro de Investigación de Métodos Computacionales (CIMEC, UNL–CONICET). Colectora RN 168 Km 472. S3000GLN Santa Fe, Argentina.*
[c] *Departamento de Ingeniería en Sistemas de Información, FRSF-UTN. Lavaise 610, Santa Fe, Argentina.*

Abstract

Lateral flow biosensors (LFB) has become a hot topic in the scientific literature in association with the rapid growing of paper-based microfluidics. Improving the existing LFB technology is a challenging task that demands large experimental efforts. Thus computer simulations are practical tools to assist the development of novel devices, since running virtual experiments considerably reduces costs and time in the path from design to real LFB prototypes. We present a computational tool for 3D numerical prototyping of LFB, which accounts for the fluid dynamics (including capillary-driven flow) in the heterogeneous porous materials, the transport of reactive components, and all the biochemical reactions involved. Mathematical modeling was carried out in the framework of continuum transport phenomena, and numerical calculations were implemented by using the finite element method. This numerical prototyping allows developers to explore arbitrary architectures, materials, and assay formats, which is demonstrated here by discussing different *real-world* examples. The advantages of the proposed numerical model are also discussed in relation to up-to-date reported methods.

Keywords: Numerical prototype, Lateral flow biosensor, Lateral flow immunoassay, paper-based microfluidics

1. Introduction

Lateral flow biosensors (LFB) here refers to the vast group of sensing techniques that have in common the fact that the test fluid is transported by capillary action in a porous substrate (nitrocellulose, filter, or chromatographic paper) and passes through a capture zone where an affinity reaction for a specific analyte takes place [1]. In this group, lateral

Email address: kler@cimec.unl.edu.ar (Pablo A. Kler)

Accepted Manuscript

ACCEPTED MANUSCRIPT

flow immunoassays are the best-established technology for rapid and easy detection of a large variety of biological markers based on the specific antigen-antibody reaction [2]. Lateral flow sensing is nowadays enlarging its application field on the base of hybridization reactions of nucleic acids [3, 4], which expand the uses to the screening of infectious diseases, food safety [5] and environmental control, among many other fields [6, 7].

The high activity currently observed in the development of LFB is motivated by several simultaneous factors. Firstly, LFB satisfy all the requirements to be implemented in resource-limited settings, mainly for public health in developing countries [8, 9]. Second, the patents that regulated the use of the base technology have been expiring during the last years, thus private or governmental institutions are now able to produce devices for a variety of new applications. A third positive factor is the coexistence with the constantly growing field of paper-based microfluidics [10, 11, 12]. And finally, the irruption of smart phones with its double function: the ability to act as optical or electrochemical reader, as well as their inherent capability for connectivity and data processing [13, 14].

In this scenario, computer simulations become a practical tool to mitigate the large experimental efforts required for new LFB development, considering that R&D processes for original and novel devices are increasingly challenging. In fact, numerical prototypes [15] of LFB would allow scientist and developers to design and explore different architectures, materials, and assay formats in the search for better binding efficiency and enhanced detection limits. Running these virtual experiments considerably reduces costs and time in the path from concept to real-world prototypes [16]. This is precisely the goal of the present work, where a complete computational model (numerical prototype) of LFB is presented.

Although numerical modeling of antigen-antibody binding in microfluidics has been under continuous development for the last ten years [17, 18, 19, 20], its employment in the development of LFB is just starting to emerge in the literature, where special attention is addressed to the influence of sample and reagent delivery formats [21, 22, 23], as well as to the effect of label particles and binding modes [24, 25, 26]. These calculations are based on commercial simulation tools, and focus on the transport and reaction problems exclusively in the reaction zone. Numerical simulations were also used lately to explore the dynamics of different membrane shapes [27], assay architectures [28], and time delays [29, 30]; these works were mostly limited to solve the 2D flow through membranes without computing binding reactions.

Accepted Manuscript

ACCEPTED MANUSCRIPT

For the particular case of lateral flow immunoassays implemented as strip tests, a 1D mathematical model was reported for sandwich [31] and competitive assays [32]. These calculations include a complete set of coupled reactions, but considering uniform and constant fluid velocity through the strip and over time. More recently, a mathematical model to predict the optimal test line location and sample volume was proposed [33], also using constant fluid velocity. Another numerical approach [34] makes use of particle filtering techniques to estimate the state of different assay parameters from experimental data of the detection line. A comprehensive review of previously reported numerical methods to simulate LFB is summarized in table S1 in the supplementary material. Finally, it is relevant to mention that analytical models of LFB have been recently published [35, 36, 37, 38]. Equations reported are very practical to explore the influence of different parameters, however they describe reactions and 1D transport processes localized in the test lines only.

Consequently with the development of the field of LFB, this work proposes the mathematical modeling, and the numerical implementation of such modeling, in order to obtain numerical prototypes able to simulate the full operation of LFB during a complete bioanalytical process. The full problem is solved in the whole 3D domain of the device, accounting for the capillary- or pressure-driven flow in each segment, the transport and diffusion of every reactive component, and the whole set of biochemical reactions involved. Mathematical modeling was carried out in the framework of continuum transport phenomena, and numerical calculations were implemented by using the finite element method (FEM). The proposal is thought to be employed as a handy tool for the design and optimization of LFB.

2. Mathematical modeling

In this section we present a compact set of equations that models all the transport phenomena present in LFB that are relevant for the assay performance, i.e. fluid dynamics, solute transport, and biochemical reactions. The modeling is based on the classical approach of porous media, where the microstructural properties of the substrates are represented by macroscopic parameters such as porosity and permeability. Besides the transport of solutes inside such structure is characterized through effective diffusion and retention coefficients.

Accepted Manuscript

ACCEPTED MANUSCRIPT

2.1. Fluid dynamic model

Here the formulation of a fluid dynamic model for the capillary imbibition of porous substrates is described. A macroscopic approach is used, where fluid velocity characteristic length is defined on an intermediate scale, which is much larger than the pore size, but smaller than the analysis domain considered, so that we avoid describing the local flow through the intricate pore space. The macroscopic flow is also assumed to be pseudo–stationary and free of inertia, in agreement with the extremely low local Reynolds numbers at pores. The system is considered to be under isothermal conditions and with controlled humidity level. Gravity is ignored in the analysis taking into account that the Bond number is negligible, but also considering the fact that LFB tests normally run horizontally.

Under these conditions, the average fluid velocity $\langle \mathbf{v} \rangle$, and the average pressure p satisfy the following equations [39, 40],

$$\nabla \cdot \langle \mathbf{v} \rangle = 0 \tag{1}$$

$$\langle \mathbf{v} \rangle = -\frac{\kappa}{\mu} \nabla p. \tag{2}$$

Equation (1) represents mass conservation for incompressible fluids that undergo neither evaporation nor condensation. Equation (2) is the well-known Darcy's law, where p is the pressure, μ is the fluid viscosity, and κ the permeability of the porous substrate (considered as a scalar, which implies material isotropy). This settings configure the most commonly used model for capillary–driven flows in paper–based substrates [27, 41, 42].

For Newtonian fluids, Eqs. (1) and (2) can be combined in order to obtain the following expression,

$$\nabla \cdot (\kappa \nabla p) = 0 \tag{3}$$

$$p = p_{sou} \qquad \text{at} \qquad \Gamma_{sou}, \tag{4}$$

$$p = p_c \qquad \text{at} \qquad \Gamma_c \tag{5}$$

where, Γ_{sou} and Γ_c are the boundary regions where source pressure (p_{sou}) is applied, and where Laplace capillary pressure (p_c) is acting over the fluid (i.e. fluid front), respectively.

Considering an arbitrary 3D flow domain, an instantaneous pressure gradient is established between regions at fluid source pressure p_{sou} and the fluid front position at pressure p_c, where the former is a characteristic function defined by the experimental conditions,

ACCEPTED MANUSCRIPT

and the last is modeled as the Laplace pressure for capillary action:

$$p_c = \frac{2\gamma cos\theta}{r_{eff}}, \tag{6}$$

where r_{eff} is the effective pore radius, γ is the air-liquid surface tension, and θ is the contact angle in the pores [43].

Regions Γ_{sou} and Γ_c are determined for every timestep, where the first one is located at the interface of the substrate with the pressure source, and the second one at the fluid front. It is worth to note that pressure source usually consist of a liquid drop at one inlet port of the device, in this case p_{sou} is the atmospheric pressure, and Γ_{sou} is the corresponding inlet port region of the substrate. This formulation also admits time-dependent pressure sources such as peristaltic pumps or hydrostatic liquid columns.

The position and geometry of Γ_c is determined with the spatial distribution of liquid saturation S in the device:

$$\Gamma_c = \{x \in \Omega_{IR^3} \quad / \quad S(x) < \sigma_{sat}\} \tag{7}$$

where Ω_{IR^3} represent the calculus domain, and σ_{sat} is a real number that represents a threshold value for defining the dry region of the substrate. Then, S is obtained by solving the following transport equation [44]:

$$\frac{\partial(S\phi)}{\partial t} + \nabla \cdot \Big(\langle \mathbf{v} \rangle S - D_S \nabla(S\phi)\Big) = 0 \tag{8}$$

where D_S is a dispersive parameter for the fluid front that is related to the microscopic properties of the substrate [45].

Finally, the pressure field for the capillary imbibition of 3D porous substrates with arbitrary porosity and permeability, is obtained by numerically solving Eq. (3) with the boundary conditions determined by Eq (8). Given the pressure field, the velocity field is obtained by solving Eq. (2).

2.2. Mass transport and chemistry

The mass transport of weakly concentrated bio-molecules can be modeled by a linear superposition of advective and diffusive transport mechanisms, plus a sink/source term due to biochemical reactions. In a non-stationary mode, the concentration of a generic

Accepted Manuscript

ACCEPTED MANUSCRIPT

species M is governed by [46]:

$$\frac{\partial([M]\phi)}{\partial t} + \nabla \cdot \Big(\alpha_M S\langle \mathbf{v}\rangle [M] - D_M \nabla([M]\phi)\Big) - r_M = 0 \tag{9}$$

were ϕ represents the porosity of the substrate, α_M is the specific retention coefficient, whose value is 1 for species that move at the advection velocity and 0 for those immobilized in the substrate matrix. Finally, D_M represents the molecular diffusion coefficient and r_M the reaction term.

In what follows we focus on antigen–antibody reactions for the formulation of numerical prototypes. In immunochemistry, the antigen (Ag) links to the binding sites of the antibody (Ab) to form an antigen-antibody complex (AgAb),

$$Ag + Ab \underset{k_u}{\overset{k_b}{\rightleftharpoons}} AgAb \tag{10}$$

where k_b and k_u are the rate constants for binding and unbinding reactions respectively. The processes of association and dissociation are much faster than the transport processes, hence, adopting chemical equilibrium constants to model the reactions between antigens and antibodies is a valid approximation. For a single antigen-antibody system, which involves three equations with the form of Eq. 9, the reactions terms to be included for Ab, Ag and AgAb, are [47]:

$$r_{Ag} = r_{Ab} = -k_b[Ag][Ab] + k_u[AgAb] \tag{11}$$

$$r_{AgAb} = k_b[Ag][Ab] - k_u[AgAb]. \tag{12}$$

It is worth to mention that Eqs. (11) and (12) are special cases for the reaction term r_M in Eq. (9). The presented numerical model is also able to deal with other biochemical reactions such as DNA hybridization, or enzymatic reactions, which are easily implemented by changing the value of r_M accordingly.

3. Numerical Simulation

3.1. Materials and methods

Computer simulations were performed by using the finite element method thorough the program PETSc-FEM [48, 49] in a Python environment. FEM is a well established and widely used numerical method for solving partial differential equations (and coupled

Accepted Manuscript

ACCEPTED MANUSCRIPT

systems of equations, as this is the case). There exists a plethora of basic and applied literature describing the method as well as its applications and capabilities [50, 51, 52]. For the particular case of the FEM implementation of the equations (1)-(12), a detailed description of the numerical procedures and their computational implementation can be found in a previous work [53].

Both 1D and 2D simulations were performed on a desktop computer with single quad-core Intel i7 7700 3.6 GHz processor, 16 GB DDR3-2400 memory, using 4 calculation threads. 3D simulations where performed by using 3 nodes (30 cores on total) of a dedicated computing cluster located at CIMEC [54]. For solving Eq.(2), as far as the resulting matrix is symmetric positive definite, we use conjugate gradients as solver, with an algebraic multigrid preconditioner, while for the set of multiple Eqs. (8) and (9), we use generalized minimal residuals as solver and the Additive Schwarz Method from the PETSc library as preconditioner.

3.2. Simulation scheme

The simulation procedure involves the iterative calculations for the coupled fields of pressure, fluid velocity, and species concentration. Once initial conditions for the flow and concentrations fields are established, the first step consists in setting an adequate timestep (Δt) for the FEM simulation. In order to determine this value, we use the following equation:

$$\Delta t = \min \left\{ \frac{\mathrm{CFL\ h_M}}{||\langle \mathbf{v} \rangle||} \right\} \tag{13}$$

where CFL accounts for the Courant-Friedrich-Levy condition [55] that we define with an optimum value of 0.45 (as a trade off between numerical stability and computing performance) and h_M is the finite element mesh parameter at the fluid front. Once the timestep is determined, one solving iteration of the transport–reaction equation system (Eqs. (8) and (9)) is performed by using the velocity field previously calculated.

The new pressure and velocity field are then recalculated (Eqs. (2) and (3)) by updating the boundary conditions, and the transport solver is called again using the updated velocity as it was previously described. This iterative scheme is reproduced until the fluid front reaches the limits of the device (the substrate is fully wet), or the fluid pumping is stopped, and consequently, velocity is null throughout the whole domain, but reaction an diffusion

ACCEPTED MANUSCRIPT

Table 1: Dimensions, material properties, initial concentrations and reactions constants of the problem used to verify the numerical tool [38].

Property	Value	Unit
Strip length	mm	40
Strip width	mm	3.5
Test line position	mm	26.7
Test line width	mm	0.8
Φ		0.7
κ	m^2	$5.5e^{-16}$
$[T]_0$	M	$1.3e^{-6}$
$[A]_0$	M	$1.66e^{-7}$
k_b	$M^{-1}\,s^{-1}$	1218.31
k_u	s^{-1}	$1.75e^{-3}$

processes are still evolving, and the transport solver continues its iteration with a default timestep related to the characteristic time of the reactions.

4. Method validation

In this section we compare the performance of our tool against experimental results from a standard lateral flow immunoassay (LFIA) test strip, available in the literature [38]. The nitrocellulose strip was modeled with the dimensions, material properties, initial concentrations and reaction constants provided in the original work and replicated in table 1. Typical results are shown in Figure 1, expressed in terms of the fraction of bound test h, that is, the amount of the test species that effectively binded the analyte, forming the AT complex, divided by the initial amount of test. The relative error between the experimental fraction of bound test $h_{Exprimental}$ and the model prediction h_{FEM} is less than 7% for $t = 300$ s. Moreover, at this relatively large reaction time, and given that test concentrations are very dilute, the analytical prediction [36, 38]:

$$h_{Analytical} = \frac{K[A]_0}{1 + K[A]_0}\left(1 - e^{(K[A]_0+1)k_u t}\right) \approx \frac{K[A]_0}{1 + K[A]_0} \tag{14}$$

where $K = k_b/k_u$, and $[A]_0$ is the initial analyte concentration, can be included for comparison (dashed line in Figure 1). It is observed that the numerical model presents a remarkable agreement with both experiments and asymptotic analytical results. Therefore, the model is exploited in next section to study more sophisticated, out of equilibrium, lateral flow assays.

ACCEPTED MANUSCRIPT

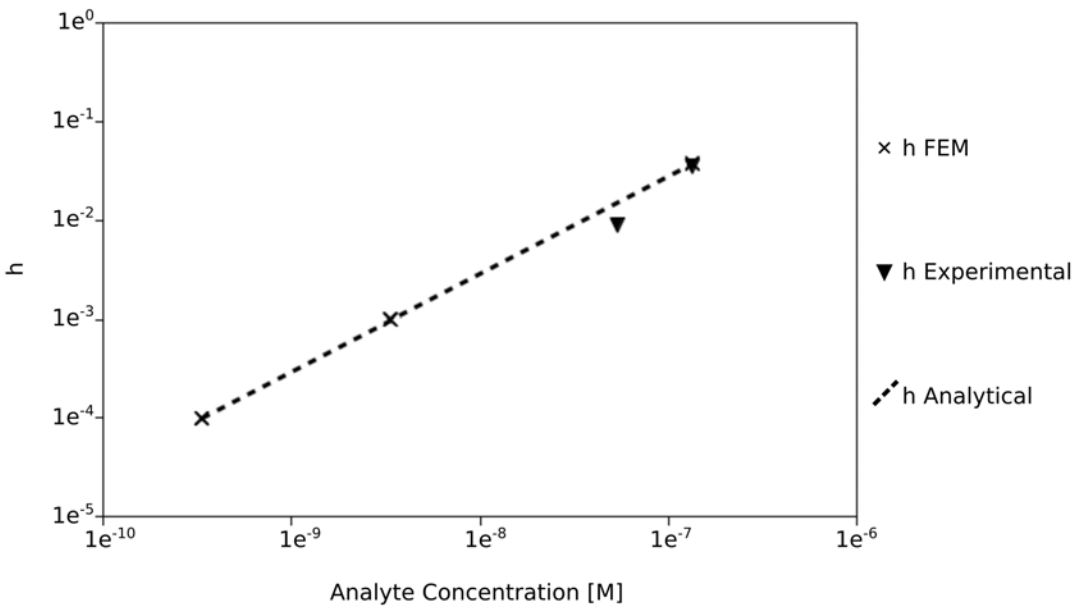

Figure 1: **Validation of the numerical tool.** The fraction of bound test h for a standard LFIA obtained with our tool (h_{FEM}) and compared with experimental results ($h_{Experimental}$) [38] and analytical models ($h_{Analytical}$) [38, 36], for $t = 300$ s.

5. Application Examples

In this section we present three application examples in order to demonstrate the tool capabilities. Such examples are presented in order of complexity, but all of them are oriented to improve the development process of LFB prototypes.

5.1. 1D numerical prototype of LFIA

One of the most widespread application of LFB is LFIA, in fact, LFIA for pregnancy test is in the market as a home diagnostic tool since many years [2]. Although information on this matter is widely available, it is worth to include here a brief description of this important family of LFB.

A typical LFIA is composed of four segments made of different porous materials, according to the function of each zone. The test begins when the sample (basically an aqueous solution containing the analyte (A)) is added to the sample pad (first segment). Capillary force drives the fluid towards the conjugate pad (second segment), where dried particles (P) are re-hydrated and mobilized by the flow. These particles work as labels for detection, and are conjugated to either antigens or antibodies (for sandwich or competitive formats, respectively), which are specifically targeted for the analyte. Immunoreactions take place while the fluid is driven through the membrane (third segment), where the capture bands are located, in order to specifically bind the molecular complex formed. The

ACCEPTED MANUSCRIPT

fluid continues towards the absorbent pad (last segment), which avoids the interruption of the flow. In the presence of analytes, the complexes captured at the test band (T) concentrates enough in order to be visible by the naked eye. A control band (C) is also included in the membrane to capture label particles.

The set of specific immunoreactions can be summarized as:

$$[A] + [P] \underset{k_{uAP}}{\overset{k_{bAP}}{\rightleftharpoons}} [AP] \tag{15}$$

$$[A] + [T] \underset{k_{uAT}}{\overset{k_{bAT}}{\rightleftharpoons}} [AT] \tag{16}$$

$$[AP] + [T] \underset{k_{uAPT}}{\overset{k_{bAPT}}{\rightleftharpoons}} [APT] \tag{17}$$

$$[P] + [C] \underset{k_{uPC}}{\overset{k_{bPC}}{\rightleftharpoons}} [PC] \tag{18}$$

$$[AP] + [C] \underset{k_{uAPC}}{\overset{k_{bAPC}}{\rightleftharpoons}} [APC] \tag{19}$$

where single letters accounts for the already described reagents, and any combination of two or three letters accounts for the corresponding complex, e.g. $[AP]$ accounts for analyte–particle complex. Non–specific reactions were not taken into account in order to facilitate the interpretation of the results, nevertheless the numerical tool is already prepared for including further reacting species.

In this first example, we present a 1D numerical prototype of a LFIA, presenting 4 segments with different porosity and permeability properties. Device dimensions, material properties and chemical properties of the species involved, where taken from literature, and are reported in Tables S2, S3 and S4 in the supplementary material. The computation domain consists of a mesh with 3000 linear segments.

Figure 2 shows the concentration profiles of every species at different times of the determination, while a complete video can be found in the supplementary material (video S1). The presented numerical experiment shows the complete operation of a typical LFIA for the case of a positive analysis. It is worth to mention that Figure 2 shows the different concentration fields, but it is not able to predict the visual perception of the user. In order to achieve this, a concentration-to-color model is required, the computation of which exceeds the aims of this work.

One may note here that, in developing a strip test, simple questions, but of significant

Accepted Manuscript

ACCEPTED MANUSCRIPT

relevance in practice, such as the optimal fluid velocity for a given capture efficiency, are usually solved via experimentation. The quantitative calculations presented here allows one to make informed decisions on the appropriate membrane porosity, capture site concentration, or sample volume, to mention a few of the several factors represented by the model parameters reported in Tables S2-S4. For this purpose, the 1D scheme adopted is quite reasonable. It should be noted that the conversion of the (real) systems with overlapped segments to one with in-plane successive zones does not necessarily mean that (real) segments are joined by the extremes; it is merely a model design to compute 1D fluid flow throughout the whole strip, and results will be compared to the 2D enriched model in the next section.

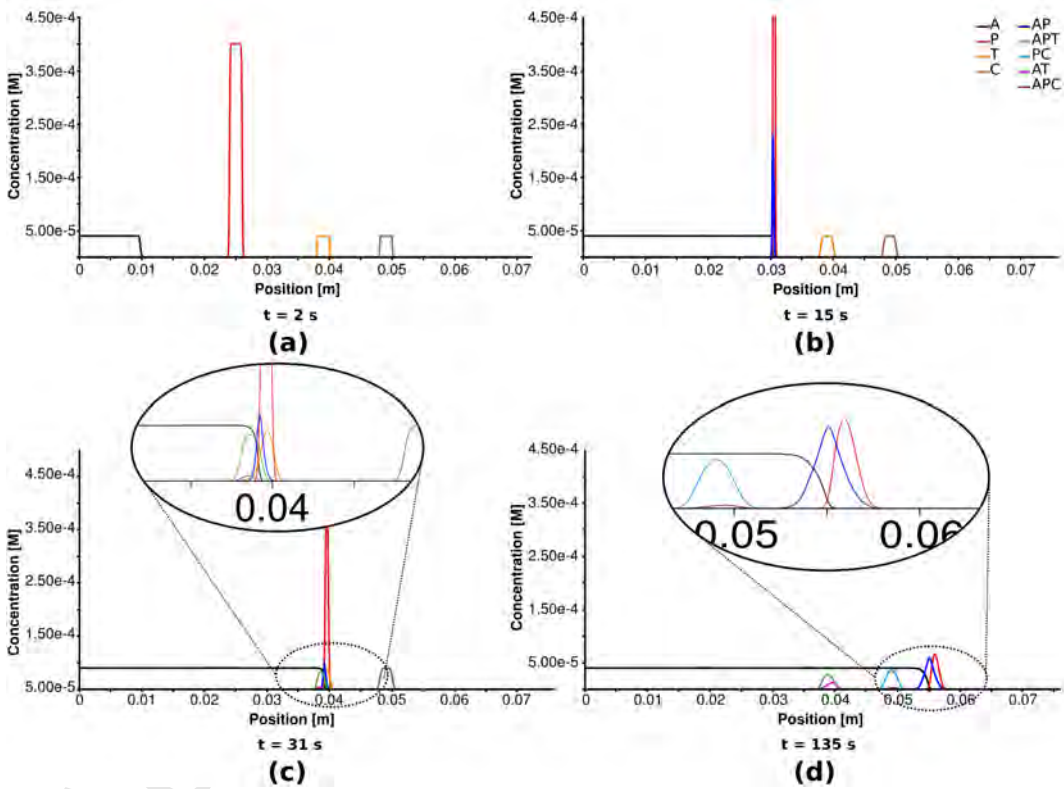

Figure 2: **Concentration profiles along the 1D strip at four different times.** (a) The analyte is transported by the flow. The label particles are still dry, as well as the test and control lines. (b) The fluid reaches the label particles. As they hydrate, they are transported by the fluid while reaction with the analyte occurs, forming the AP complex. (c) The fluid reaches the test line and the reaction with A and AP begins, forming AT and APT. (d) The fluid passes through the control line and continues to the absorbent pad. The complex PC and APC indicate the validity of the (virtual) test performed.

5.2. 2D numerical prototype of LFIA

In this example, the previous prototype is re-calculated in a 2D domain, in order to capture the influence of the 2D flow in the regions of material overlap between segments. In this case, the computation domain consists of a mesh with 150440 quadrilateral lin-

ACCEPTED MANUSCRIPT

ear elements, while material properties, initial concentrations, reaction constants of the chemical species involved, and dimensions of the device are exactly the same than in the previous example, except the strip height, which was not considered previously, and equals 500 µm. Figure 3 summarizes the obtained numerical results, while a complete video of the operation of the prototype is reported in the supplementary material (video S2).

It is worth noting that all the results regarding concentration fields are perfectly comparable with the previous 1D prototype, besides a slight difference for the arriving time due to the increase of the effective pathlength due to the material overlap. In fact, in addition to the information provided by the 1D model discussed above, this calculation allows one to investigate the influence of the 2D streamlines on the assay performance. More precisely, it is of interest to achieve an efficient transport of the different reactants in the search for better analyte capture. Figure 3(b) clearly shows the perturbations that the plug of particles undergoes while passing the overlapping zone between the conjugate pad and the membrane. This simple example suggests that there is space to improve the sensitivity and detection limits by redesigning the connection between segments. This aspect is further discussed in the next study case.

5.3. Full 3D numerical prototype of LFB for dengue detection

The last application example consists in a full 3D numerical prototype of the LFB for the detection of dengue-specific immunoglobulins, recently reported by [56]. In this LFB, the sample (salivary fluid) and the regent are conducted through different paths: the former is placed in the sample pad, where several unwanted proteins are filtered, and meets the reagent upstream in a common strip (membrane). The analyte and the particles react to form the AP complex directly on the membrane, where test and a control line are located. At the end of the device, the absorbent pad enables a continuous flow that increases the amount of APT and PC formed. The numerical prototype was constructed by using the geometry detailed in the original work [56] and meshed with 127690 hexahedral linear elements. Properties of the material and the chemical species involved, are reported in Tables S5 and S6 in the supplementary material.

Zang and co-workers evaluated two possible configurations: in the first one, the sample and conjugate pads where directly laid on the test strip, producing a typical *side flow* profile (Figure 4(a)), which yielded uneven reactions in the detection section of the test strip, as is shown in Figure 5(a). In the second configuration, an impermeable membrane

ACCEPTED MANUSCRIPT

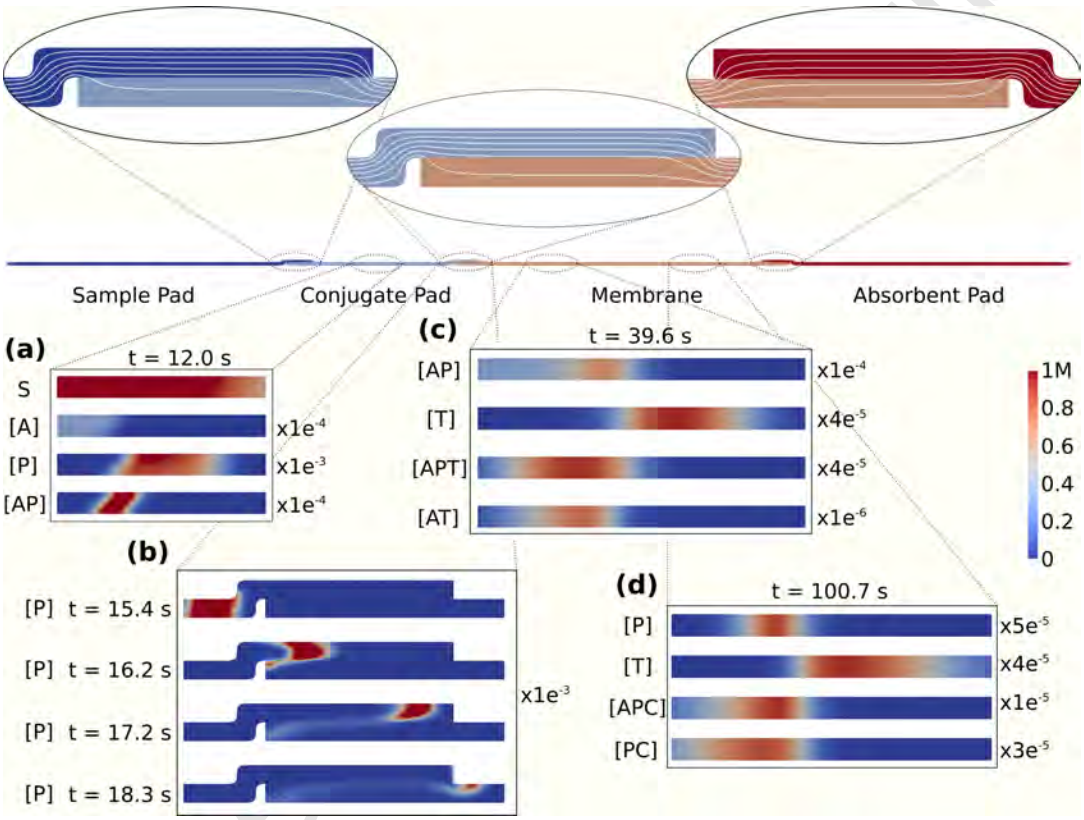

Figure 3: **Fluid velocity and concentration profiles along the 2D strip at different times.** The top of the figure shows the streamlines in the overlapping regions between segments. In the bottom, relevant concentration profiles are depicted. (a) At $t = 12s$ the label particles are hydrated, and the [A]+[P]⇌[AP] reaction begins. (b) From $t = 15.3$ to $t = 18.3s$, the particles arrive to the first overlapping region, and they are spread due to the local velocity profile. (c) At $t = 39.6s$, P and AP arrive to the test line, and the [A]+[T]⇌[AT] and [AP]+[T]⇌[APT] reactions take place. (d) At $t = 100.7$ the remaining P and AP arrive to the control line, forming the complexes PC and APC.

ACCEPTED MANUSCRIPT

was placed between the conjugate and the sample pads, in order to separate both streams (Figure 4(b)). This configuration produced a *stacking flow* profile which resulted in even AP concentrations, and thus, even reactions in the detection lines as is shown in Figure 5(b). Additionally, it is worth to mention that Figure 5 clearly shows the capability of the numerical prototype for reproducing the experimental results in both configurations. It is also evident that the response of different designs can be easily predicted by running the numerical prototype without the need of large experimental effort.

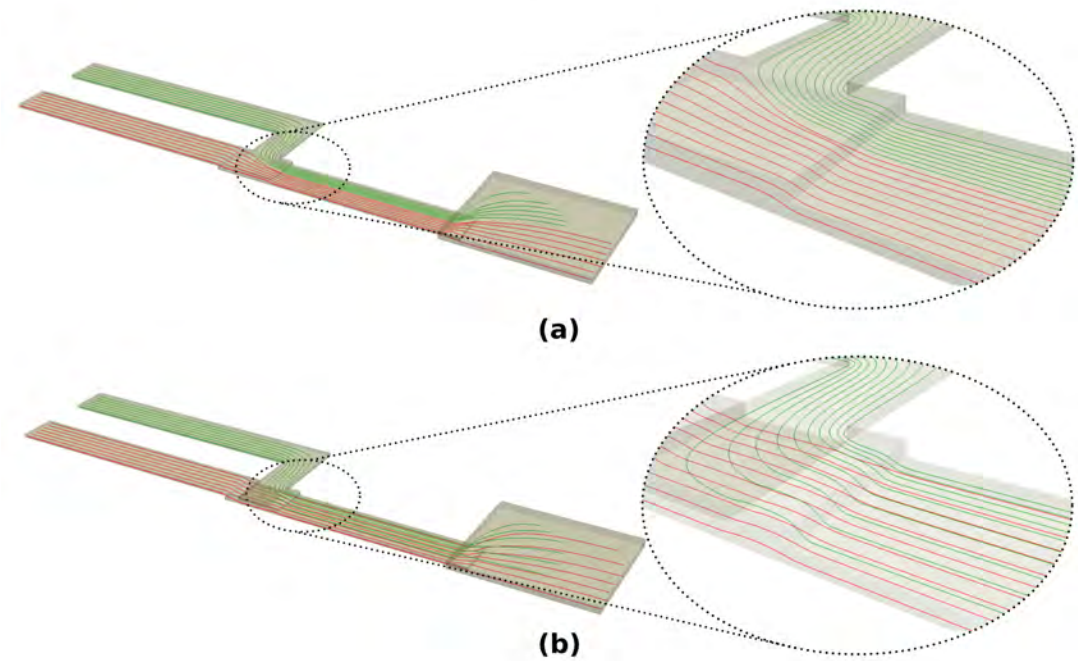

Figure 4: **3D flow profiles.** (a) *Side flow* streamlines obtained when no impermeable membrane is used between the sample and conjugate pads. (b) Streamlines in the *stacking flow* obtained when the impermeable membrane is used to isolate the sample and conjugate pads flows. In both cases, the flow developed in the sample pad is indicated with red streamlines, while green is used for streamlines originated in the conjugate pad.

The full operation procedure of this LFB was also simulated. Results obtained numerically at five relevant times, are shown in Figure 6 and a complete video of the operation of the prototype can be found in the supplementary material (video S3).

As seen in Figure 6, the sharp corners of the sample pad produce a large distortion in the traveling particle band. In order to illustrate the high potential of numerical prototyping, the geometry was optimized to improve the transport of the detection particles as it is shown in Figure 7. The geometry was re-designed by following a previous work [57] which shows how to minimize the racetrack effect. Figure 7 shows that such optimization allows both a faster transport of the particle band and a better seizing of them. In fact, after 75s, more than 98% of the available particles has crossed the outlet plane in the optimized

ACCEPTED MANUSCRIPT

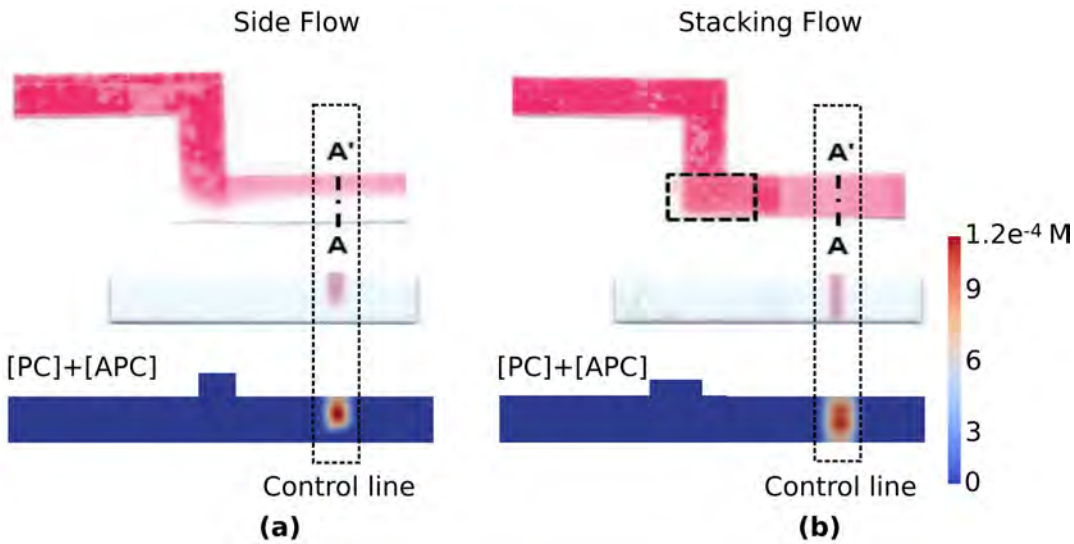

Figure 5: **Control line reaction with stacking and side flows.** (a) Even control line obtained with the stacking flow approach. (b) Uneven control line obtained with side flow. The top images are adapted from [56] with permission of the Royal Society of Chemistry. The bottom figures are the concentration profiles obtained numerically in this work.

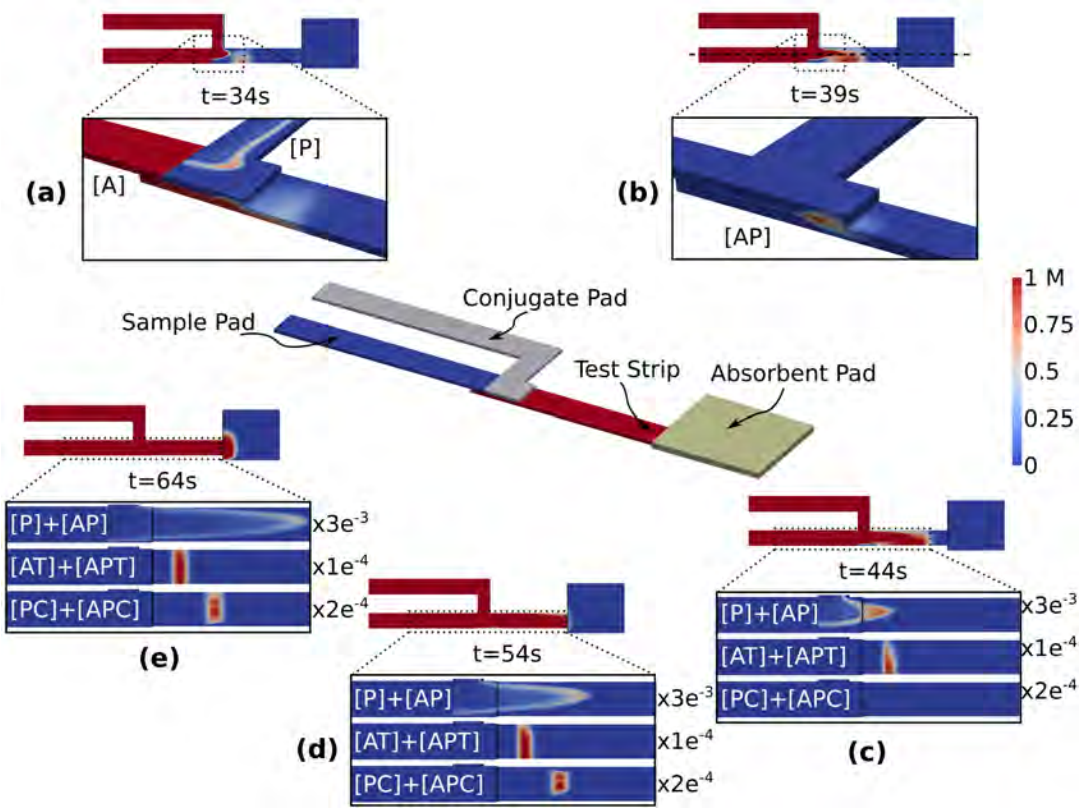

Figure 6: **Concentration profiles along the 3D LFB at different times.** The layout of the device is depicted in the centre of the figure. (a) At t=34 s the two fluid fronts containing the analyte and the detection particles are close to reach the test strip. (b) At t=39 s, both fronts meet and the AP complex formation begins. (c) When t=44 s; AP, P, and A, arrive to the test line, and react with T. (d) At t=54 s the front reach the control line, forming PC and APC. (e) t=64 s, the front has reached the absorbent pad, and the test and control zones are almost totally formed.

ACCEPTED MANUSCRIPT

geometry. On the other hand, in the sharp edged geometry, after 95 s, more than 10% of the available particles are behind the same plane. Moreover, the optimized geometry produces a neater particle band, and hence neater reactions in the test strip. Finally, the new design can be fabricated with the same laser tool used by the authors [56], and fits in the same original cassette. A complete video of this numerical experiment is reported in the supplementary material (video S4).

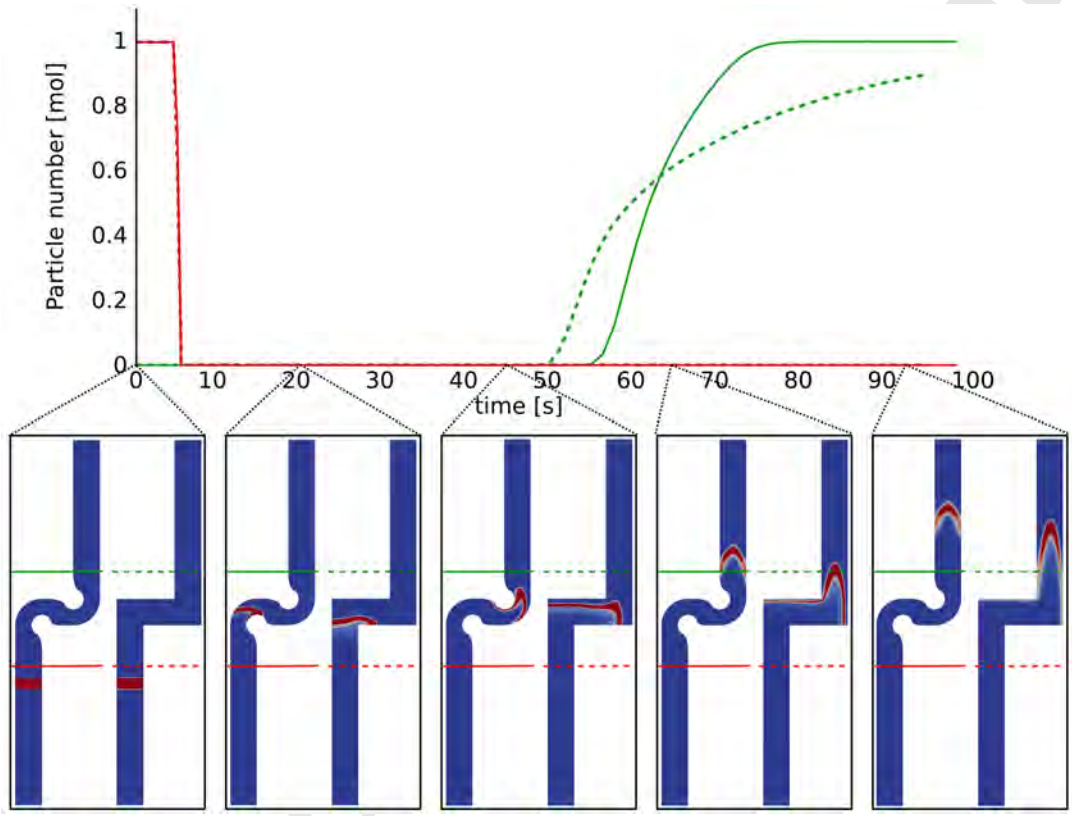

Figure 7: **Conjugate pad geometry optimization.** In the top of the figure, the amount of particles present in the conjugate pad, up to the red plane, is plotted in red against time. Similarly, the amount of particles, measured in mols, which already crossed the green plane, is plotted in green. In both cases, solid lines correspond to the optimized-curved geometry, while the dashed lines correspond to the sharp-edged geometry. In the bottom of the figure, particle band distortion, at five relevant times, is shown for both geometries.

6. Conclusions

In this work we have developed a robust model that configures a complete and realistic numerical prototype for LFB which is able to simulate a wide range of practical situations. We have compared the performance of our method against analytical predictions and experimental results from a standard LFIA available in the literature, in order to validate the proposed numerical prototyping tool. In the first and second application examples, we have described the operation principles of a typical LFIA. The examples present two approach

ACCEPTED MANUSCRIPT

levels: the 1D prototype enables a fast resolution of the model and a rough estimation of the main design parameters such as substrate lengths, reactive concentrations, placement of the test and control lines, and general assay times. The 2D prototype provides more specific information in order to assist a more advanced stage of a prototype design, and the optimization of geometrical parameters, such as the shape of pathlines dispersing the sample plug. In the third example, the 3D model gathered all these phenomena, but in a more complex configuration for an already launched prototype, enabling to discuss further optimization, based on experimental results. The different possible approaching levels of the presented tool enables researchers to deal with the design problem of LFB at different stages of their development, from a preliminary concept to the redesign of a consolidated device.

Finally, one may conclude that the numerical prototypes are capable to deal with 3D geometrical configurations, as well as with the variation of several physicochemical and operational parameters that determine the LFB performance, i.e., porosity (materials and geometric distribution), reactants concentrations, spatial distribution of bands, solubility of compounds, velocity reactions, fluid viscosity, etc. This allows one to optimize the operation of already available devices, and opens a wide range of new possibilities, like running batch sensibility tests, or more interestingly, the prototyping of totally new devices. Concerning detection, it is worth noting that the output of our calculations is the concentration profile of each species during the assay. At the end of the test, one could appropriately convert this concentrations into different physical signals such as typical light absorbance or fluorescence. This possibility is of much interest for the simulation of LFB that makes use of external readout, for example electrochemical detection or cell phone based optical readings. This research topic is currently under development in our working group.

Conflicts of interest

All authors declare complete absence of financial/commercial conflicts of interest.

Acknowledgements

Authors want to acknowledge CONICET (PIP 0363), UNL(CAI+D 50420150100030LI), UTN (PID4475), ASACTEI (AC00010-18, Res. 117/14), and ANPCyT, Argentina for the financial support, and Alejandro Dabin at C^3 (CIMEC) for his valuable collaboration.

Accepted Manuscript

ACCEPTED MANUSCRIPT

References

[1] D. Quesada-González, A. Merkoçi, Nanoparticle-based lateral flow biosensors, Biosens Bioelectron 73 (2015) 47–63.

[2] R. Wong, H. Tse (Eds.), Lateral Flow Immunoassay, Humana Press, New York, 2009.

[3] Z. Fang, W. Wu, X. Lu, L. Zeng, Lateral flow biosensor for dna extraction-free detection of salmonella based on aptamer mediated strand displacement amplification, Biosens Bioelectron 56 (2014) 192–197.

[4] X. Gao, H. Xu, M. Baloda, A. S. Gurung, L.-P. Xu, T. Wang, X. Zhang, G. Liu, Visual detection of microrna with lateral flow nucleic acid biosensor, Biosens Bioelectron 54 (2014) 578–584.

[5] M. J. Raeisossadati, N. M. Danesh, F. Borna, M. Gholamzad, M. Ramezani, K. Abnous, S. M. Taghdisi, Lateral flow based immunobiosensors for detection of food contaminants, Biosens Bioelectron 86 (2016) 235 – 246.

[6] Y. Du, S. Dong, Nucleic acid biosensors: Recent advances and perspectives, Anal. Chem 89 (2017) 189–215.

[7] S. Neethirajan, S. K. Tuteja, S.-T. Huang, D. Kelton, Recent advancement in biosensors technology for animal and livestock health management, Biosens Bioelectron 98 (2017) 398 – 407.

[8] P. Yager, T. Edwards, E. Fu, K. Helton, K. Nelson, M. R. Tam, B. H. Weigl, Microfluidic diagnostic technologies for global public health, Nature 442 (2006) 412–418.

[9] G. A. Posthuma-Trumpie, J. Korf, A. van Amerongen, Lateral flow (immuno) assay: its strengths, weaknesses, opportunities and threats. a literature survey, Anal. Bioanal. Chem. 393 (2009) 569–582.

[10] X. Li, D. R. Ballerini, W. Shen, A perspective on paper-based microfluidics: current status and future trends, Biomicrofluidics 6 (2012) 011301.

[11] A. K. Yetisen, M. S. Akram, C. R. Lowe, Paper-based microfluidic point-of-care diagnostic devices, Lab Chip 13 (2013) 2210–2251.

[12] D. M. Cate, J. A. Adkins, J. Mettakoonpitak, C. S. Henry, Recent developments in paper-based microfluidic devices, Anal. Chem. 87 (2015) 19–41.

Accepted Manuscript

ACCEPTED MANUSCRIPT

[13] D. Erickson, D. O'Dell, L. Jiang, V. Oncescu, A. Gumus, S. Lee, M. Mancuso, S. Mehta, Smartphone technology can be transformative to the deployment of lab-on-chip diagnostics, Lab Chip 14 (2014) 3159–3164.

[14] D. Quesada-González, A. Merkoçi, Mobile phone-based biosensing: An emerging diagnostic and communication technology, Biosens Bioelectron 92 (2017) 549 – 562.

[15] D. Erickson, Towards numerical prototyping of labs-on-chip: modeling for integrated microfluidic devices, Microfluid. Nanofluid. 1 (2005) 301–318.

[16] P. A. Kler, C. L. Berli, F. A. Guarnieri, Modeling and high performance simulation of electrophoretic techniques in microfluidic chips, Microfluid. Nanofluid. 10 (2011) 187–198.

[17] G. Hu, Y. Gao, D. Li, Modeling micropatterned antigen–antibody binding kinetics in a microfluidic chip, Biosens Bioelectron 22 (2007) 1403–1409.

[18] H. Parsa, C. D. Chin, P. Mongkolwisetwara, B. W. Lee, J. J. Wang, S. K. Sia, Effect of volume-and time-based constraints on capture of analytes in microfluidic heterogeneous immunoassays, Lab Chip 8 (2008) 2062–2070.

[19] T. M. Squires, R. J. Messinger, S. R. Manalis, Making it stick: convection, reaction and diffusion in surface-based biosensors, Nature biotech 26 (2008) 417–426.

[20] E. Fu, K. E. Nelson, S. A. Ramsey, J. O. Foley, K. Helton, P. Yager, Modeling of a competitive microfluidic heterogeneous immunoassay: sensitivity of the assay response to varying system parameters, Anal Chem 81 (2009) 3407–3413.

[21] J. Chou, L. E. Li, E. Kulla, N. Christodoulides, P. N. Floriano, J. T. McDevitt, Effects of sample delivery on analyte capture in porous bead sensors, Lab Chip 12 (2012) 5249–5256.

[22] D. Gasperino, B. Grant, J. Dantzler, W. B., Supporting high-sensitivity lateral flow assay development through predictive modeling, in: 20th International Conference on Miniaturized Systems for Chemistry and Life Sciences, MicroTAS 2016, 2016, pp. 792–793.

Accepted Manuscript

ACCEPTED MANUSCRIPT

[23] T. Liang, R. Robinson, J. Houghtaling, G. Fridley, S. A. Ramsey, E. Fu, Investigation of reagent delivery formats in a multivalent malaria sandwich immunoassay and implications for assay performance, Anal Chem 88 (2016) 2311–2320.

[24] Z. Liu, J. Hu, A. Li, S. Feng, Z. Qu, F. Xu, The effect of report particle properties on lateral flow assays: A mathematical model, Sensor Actuat B-Chem 248 (2017) 699–707.

[25] J. Kim, R. Poling-Skutvik, J. R. Trabuco, K. Kourentzi, R. C. Willson, J. C. Conrad, Orientational binding modes of reporters in a viral-nanoparticle lateral flow assay, Analyst 142 (1) (2017) 55–64.

[26] G. L. Mosley, P. Nguyen, B. M. Wu, D. T. Kamei, Development of quantitative radioactive methodologies on paper to determine important lateral-flow immunoassay parameters, Lab Chip 16 (15) (2016) 2871–2881.

[27] S. Mendez, E. M. Fenton, G. R. Gallegos, D. N. Petsev, S. S. Sibbett, H. A. Stone, Y. Zhang, G. P. López, Imbibition in porous membranes of complex shape: quasi-stationary flow in thin rectangular segments, Langmuir 26 (2009) 1380–1385.

[28] C. Parolo, M. Medina-Sánchez, A. de la Escosura-Muñiz, A. Merkoçi, Simple paper architecture modifications lead to enhanced sensitivity in nanoparticle based lateral flow immunoassays, Lab Chip 13 (2013) 386–390.

[29] L. Rivas, M. Medina-Sánchez, A. de la Escosura-Muñiz, A. Merkoçi, Improving sensitivity of gold nanoparticles-based lateral flow assays by using wax-printed pillars as delay barriers of microfluidics, Lab Chip 14 (2014) 4406–4414.

[30] J. R. Choi, Z. Liu, J. Hu, R. Tang, Y. Gong, S. Feng, H. Ren, T. Wen, H. Yang, Z. Qu, et al., Polydimethylsiloxane-paper hybrid lateral flow assay for highly sensitive point-of-care nucleic acid testing, Anal Chem 88 (2016) 6254–6264.

[31] S. Qian, H. H. Bau, A mathematical model of lateral flow bioreactions applied to sandwich assays, Anal. Biochem. 322 (2003) 89–98.

[32] S. Qian, H. H. Bau, Analysis of lateral flow biodetectors: competitive format, Anal. Biochem. 326 (2004) 211–224.

Accepted Manuscript

ACCEPTED MANUSCRIPT

[33] M. Ragavendar, C. M. Anmol, A mathematical model to predict the optimal test line location and sample volume for lateral flow immunoassays, in: Engineering in Medicine and Biology Society (EMBC), 2012 Annual International Conference of the IEEE, IEEE, 2012, pp. 2408–2411.

[34] N. Zeng, Z. Wang, Y. Li, M. Du, X. Liu, Identification of nonlinear lateral flow immunoassay state-space models via particle filter approach, IEEE Trans. Namonthch 11 (2012) 321–327.

[35] D. V. Sotnikov, A. V. Zherdev, B. B. Dzantiev, Mathematical model of serodiagnostic immunochromatographic assay, Anal Chem 89 (2017) 4419–4427.

[36] C. L. Berli, P. A. Kler, A quantitative model for lateral flow assays, Microfluid Nanofluid 20 (2016) 1–9.

[37] H. V. Hsieh, J. L. Dantzler, B. H. Weigl, Analytical tools to improve optimization procedures for lateral flow assays, Diagnostics 7 (2) (2017) 29.

[38] B. Y. Moghadam, K. T. Connelly, J. D. Posner, Two orders of magnitude improvement in detection limit of lateral flow assays using isotachophoresis, Anal Chem 87 (2) (2015) 1009–1017.

[39] A. Szymkiewicz, Modelling water flow in unsaturated porous media: accounting for nonlinear permeability and material heterogeneity, Springer Science & Business Media, 2012.

[40] R. Masoodi, K. M. Pillai, Wicking in porous materials: traditional and modern modeling approaches, CRC Press, 2012.

[41] J. Hyväluoma, P. Raiskinmäki, A. Jäsberg, A. Koponen, M. Kataja, J. Timonen, Simulation of liquid penetration in paper, Phys. Rev. E 73 (2006) 036705.

[42] E. Elizalde, R. Urteaga, C. L. Berli, Rational design of capillary-driven flows for paper-based microfluidics, Lab Chip 15 (2015) 2173–2180.

[43] P.-G. de Gennes, F. Brochard-Wyart, D. Quere, Capillarity and wetting Phenomena, Springer-Verlag, New York, 2004.

[44] E. Thompson, Use of pseudo-concentrations to follow creeping viscous flows during transient analysis, Int. J. Numer. Methods Fluids 6 (1986) 749–761.

Accepted Manuscript

ACCEPTED MANUSCRIPT

[45] S. Gruener, Z. Sadjadi, H. E. Hermes, A. V. Kityk, K. Knorr, S. U. Egelhaaf, H. Rieger, P. Huber, Anomalous front broadening during spontaneous imbibition in a matrix with elongated pores, Proceedings of the National Academy of Sciences 109 (2012) 10245–10250.

[46] H. Gerke, M. V. Genuchten, A dual-porosity model for simulating the preferential movement of water and solutes in structured porous media, Water resources research 29 (1993) 305–319.

[47] D. Wild, The Immunoassay Handbook, Elsevier Science Ltd, 2005.

[48] L. D. Dalcin, R. R. Paz, P. A. Kler, A. Cosimo, Parallel distributed computing using python, Adv. Water Resour. 34 (2011) 1124–1139.

[49] P. A. Kler, E. J. López, L. D. Dalcín, F. A. Guarnieri, M. A. Storti, High performance simulations of electrokinetic flow and transport in microfluidic chips, Computer Methods in Applied Mechanics and Engineering 198 (30) (2009) 2360–2367.

[50] K.-J. Bathe, Finite element method, Wiley Online Library, 2008.

[51] O. C. Zienkiewicz, R. L. Taylor, The finite element method, Vol. 3, McGraw-hill London, 1977.

[52] T. J. Hughes, The finite element method: linear static and dynamic finite element analysis, Courier Corporation, 2012.

[53] P. A. Kler, L. D. Dalcin, R. R. Paz, T. E. Tezduyar, Supg and discontinuity-capturing methods for coupled fluid mechanics and electrochemical transport problems, Comput. Mech. 51 (2013) 171–185.

[54] Pirayú, ASACTEI, http://www.cimec.org.ar/c3/pirayu/equipos.php (2016).

[55] J. Donea, A. Huerta, Finite Element Methods for Flow Problems, Wiley Online Library, 2003.

[56] Y. Zhang, J. Bai, J. Y. Ying, A stacking flow immunoassay for the detection of dengue-specific immunoglobulins in salivary fluid, Lab Chip 15 (2015) 1465–1471.

[57] J. I. Molho, A. E. Herr, B. P. Mosier, J. G. Santiago, T. W. Kenny, R. A. Brennen, G. B. Gordon, B. Mohammadi, Optimization of turn geometries for microchip electrophoresis, Anal Chem 73 (2001) 1350–1360.

Accepted Manuscript

ACCEPTED MANUSCRIPT

Federico Schaumburg is a posdoc researcher at the Institute of Technological Development for the Chemical Industry (INTEC), at the National Council of Scientific and Technical Research (CONICET) and the Universidad Nacional del Litoral (UNL) in Santa Fe, Argentina. He finished his PhD studies in march 2017, in which he developed numerical models for the dosimetry and electromagnetic compatibillity of implantable BioMEMS devices. Currently he joined the Santa Fe Microfluidics Group (GSaM), where he works modelling different aspects of the paper-based microfluidic devices.

Pablo A. Kler is a research scientist at the Research Center for Computational Methods (CIMEC), at the Universidad Nacional del Litoral in Santa Fe, Argentina. He is also assistant Professor of the Informatics System Engineering department at the Universidad Tecnológica Nacional. Prof. Kler has been working since 2005 on modeling and simulations of microfludics and transport phenomena at the microscale, with emphasis on electromigrative separation techniques for standard and "Lab-on-a-chip" platforms. Currently he is developing computational tools for the optimization of different analytical techniques including 2D/CE-MS and paper-based LFIA.

Claudio L.A. Berli received a bachelor's degree in Biochemistry and PhD in Chemical Technology from National University of Litoral (UNL), Argentina, then held a postdoctoral position at the University of Paris, in the field of Physicochemical Hydrodynamics. Currently he is Full Professor at the Department of Basic Sciences, UNL, and Researcher of the National Council for Scientific and Technological Investigations (CONICET), at INTEC, Santa Fe, Argentina. His research interests include Microfluidics, Electrokinetics, and Lab-on-a-Chip devices.

Accepted Manuscript

ACCEPTED MANUSCRIPT

Paper Highlights. Numerical prototyping of lateral flow biosensors.

Federico Schaumburg, Pablo A. Kler and Claudio L. A. Berli

A novel complete numerical prototyping of lateral flow biosensors is presented.

Full transport problem in 3D paper-based microfluidic devices is considered.

The model enables LFB design with different geometries and assay formats.

Better binding efficiency, shorter assay times, or improved LODs are readily explored.

Accepted Manuscript